Università degli Studi di Napoli "Federico II"

SCUOLA POLITECNICA E DELLE SCIENZE DI BASE

DIPARTIMENTO DI INGEGNERIA INDUSTRIALE

CORSO DI LAUREA IN INGEGNERIA AEROSPAZIALE

CLASSE DELLE LAUREE IN INGEGNERIA INDUSTRIALE (L-9)

Elaborato di laurea in Meccanica del Volo

"Wind tunnel data processing of a wing with flap and distributed propellers"

Relatore:
Prof. Danilo Ciliberti

Candidato:
Angelo Viscovo

ANNO ACCADEMICO 2023 – 2024

Ai miei cari nonni:
Mario e Antonietta,
sempre presenti nel mio
cuore allora come oggi.

Abstract

This paper focuses on aero-propulsive interactions generated by distributed propulsion. The objective consists in a post-processing of wind tunnel data collected from experiments on a finite flapped wing, equipped with three electric propellers mounted on its leading edge. Experimental measurements were recorded at various angles of attack, angular velocities and propellers' array positions. Using these data, the total forces and the total pitching moment acting on the wing were reconstructed, including the contributions from propulsive forces coming from thrust and normal force generated by the individual propellers. From these results, the total lift, drag and pitching moment coefficients were obtained in order to describe the effects of distributed propulsion on wing aerodynamics. The analysis conducted in this first part of the paper accounted for both indirect and direct propulsive effects, which were actually contained within the total forces and the total pitching moment expressions. Subsequently, the influence of the relative positioning of the propellers' array was evaluated for four different configurations. Finally, numerical data deriving from CFD simulations were utilized to remove propulsive effects from the expressions of total forces and moments. By applying an inverse process to the total forces (and moment), the indirect effects of distributed propulsion were isolated, allowing for a clearer representation of its impact on the wing aerodynamics. This approach provided a more precise understanding of the role of distributed propulsion, completely excluding the effects of direct propulsive contributions.

Sommario

Questo elaborato si concentra sulle interazioni aero-propulsive generate dalla propulsione distribuita. L'obiettivo consiste nella rielaborazione, in post-processing, di dati raccolti in galleria del vento durante esperimenti su di un'ala finita dotata di flap ed equipaggiata con tre eliche (mosse da motori elettrici) montate sul bordo d'attacco. Le misure sperimentali sono state registrate a diversi angoli di attacco, velocità angolari e posizioni delle eliche. Utilizzando questi dati, sono state ricostruite le forze e il momento di beccheggio totali agenti sull'ala, includendo i contributi delle forze propulsive derivanti dalla spinta e dalla forza normale generate dalle singole eliche. Successivamente sono stati ottenuti i coefficienti aerodinamici totali di portanza, resistenza e momento di beccheggio, per descrivere gli effetti della propulsione distribuita sull'aerodinamica dell'ala. L'analisi svolta in questa prima parte dell'elaborato ha tenuto conto sia degli effetti propulsivi indiretti sia di quelli diretti, effettivamente contenuti all'interno delle espressioni delle forze e del momento totale. Successivamente, è stata valutata l'influenza della posizione relativa delle eliche per quattro diverse configurazioni. Infine, dati numerici derivanti da simulazioni CFD sono stati utilizzati per rimuovere gli effetti propulsivi dalle espressioni delle forze totali e del momento totale. Utilizzando un processo inverso applicato alle forze totali (ed al momento totale), sono stati isolati gli effetti indiretti della propulsione distribuita, consentendo una rappresentazione più chiara del suo impatto sull'aerodinamica dell'ala. Questo approccio ha così fornito una comprensione più precisa del ruolo della propulsione distribuita, escludendo completamente gli effetti delle componenti propulsive dirette.

Table of contents

List of figures

List of tables

1. Introduction

Distributed Propulsion consists in a propulsion system where the vehicle thrust is produced from an array of propulsors located across the air vehicle, or in general along its wings. The purpose of this innovating idea is to improve aircraft's aerodynamic, propulsive and/or structural efficiency over an equivalent conventional design, leading to new and unprecedented benefits.

This concept also expands to DEP (Distributed Electric Propulsion), a system where electrical energy sources are connected via transmission lines to multiple electric motor-driven propulsors. Benefits include improved fuel efficiency, emissions, noise, landing field length handling and also the potential to introduce substantial improvements in future air-vehicle performance, efficiency, and robustness. Moreover, as DEP configuration aircrafts use electricity as energy source, DEP itself can also open up to a greener and non-polluting solution.

During the last decade, distributed propulsion has been one of the most investigated technologies. Even in the last few years several Unmanned Aerial Vehicle (UAV) projects have explored the potential of distributed propulsion to offer noise abatement, fuel efficiency and short-field performance.

Indeed, the effects of distributed propulsion are still being studied up to this day, searching for new improvements and solutions to increase aircrafts' performances in cruise and most importantly at lower speeds. At low speeds, velocity definitely becomes less significant with respect to the lift coefficient, as most of the lift produced comes from the augmentation of the latter, usually with high lift devices. Distributed propulsion could be seen with same conception, actively augmenting lift during take-off and landing.

In fact, multiple propulsors are mounted to, not only produce thrust, but also yield beneficial aerodynamic-propulsion interaction (aero-propulsive effects). A wide research has been conducted to describe these effects, which lead to possible benefits but also to negative consequences. Analyses were mostly done using semispan wings with at least three propellers displaced along the leading edge.

Some studies refer to different propellers' array positions (moving it horizontally and vertically) along the wing in three different flight configurations (take-off, cruise, landing) in order to highlight the most advantageous positions to locally increase the dynamic pressure q_∞ and the lift coefficient C_L. Numerical investigations clearly show that the most efficient positions of the propellers' array changed depending on the trailing edge flap configurations (referring to the different phases of flight) [1].

Some others focus on propellers' inclination leading to the realization of the possibility to increase the lift coefficient, shifting its curve or even changing the lift curve slope $C_{L\alpha}$. As imaginable, vertical displacements of the propellers' array showed more effective lift augmentation than longitudinal displacements. Whereas decreasing the nacelle inclination (increased pitch-down) increased the lift performance of the flapped system over the entire angle of attack range. The combination of large pitch-down inclination angle and high angle of attack showed the largest increase in lift increment [2].

Any possible lift augmentation is always accompanied by a drag increase due to the presence of lift induced drag, at first glance, proportional to the square of the lift coefficient C_L^2. DEP or in general DP can also be used intelligently to reduce this negative effect by mounting propellers at the wingtips, letting them rotate opposite to the wingtip vortices. This can induce a vorticity weakening, leading to a less intense effect of the augmentation of drag.

In fact, mounting propellers on the wingtips can lead to a considerable decrease of induced drag. Studies have been conducted using different propeller diameters larger than 1.0 m, at different RPM to observe the effects on the drag coefficient C_D. Results show that induced drag could be reduced up to 10% in a specific range of C_L, increasing the high lift capabilities of about 20% (flap up) and 60-80% (flap down). Tip propeller diameter must be properly dimensioned according to the nacelle size and thrust settings to optimize drag reduction [3].

An even further application of Distributed Electric Propulsion links to PCA, which stands for "Propulsion Controlled Aircraft": airplanes where rotations around x_B, y_B, z_B (roll, pitch and yaw around the axes of the body-reference frame) can be controlled by adjustments to the propulsors, rather than traditional control surfaces. This can increase influence on the aircraft's total forces and moments, potentially even leading to the elimination of more traditional control surfaces, decreasing the overall weight of the whole aircraft [4].

It is clear that DP (and also DEP) can guarantee higher lift coefficients, improving the wing design and aircraft performance. They surely bring many potential unprecedented benefits but also come with their own set of challenges and limitations, that still stop them from being introduced into production as innovating propulsive systems. Although the implementation of such technologies may still be something unfeasible today, DP (or DEP) can definitely be (and definitely are) a very interesting field of research for future aircraft design concepts.

In this paper, there will be a more distinct focus on aero-propulsive interactions generated by distributed propulsion. Data obtained from several previous wind tunnel experiments on a flapped wing with distributed propellers will be analyzed. During the experimental tests, the electric propellers have been positioned in different configurations along the wing, at different RPM and angles of attack, independently generating different values of thrust, normal force, lift and drag.

A subsequent post-processing will be done, in order to obtain the total forces and moments on the wing, leading to the decoupling of the aerodynamic effects given by distributing the propellers along the wing from the propulsive effects of the engines themselves. In this way direct effects of distributed propulsion will become even more evident.

2. Experimental setup

The conducted experiments examine wind tunnel test outcomes for a wing equipped with a flap and three distributed high-lift propellers. These propellers were adjusted along the longitudinal plane to assess how varying their position relative to the wing influences performance. Prior to testing, preliminary numerical analyses were conducted to identify the most promising configurations to be tested in the wind tunnel.

To account for all relevant aerodynamic effects, the model featured strain gauge balances on both the wing and motors, along with pressure taps on selected sections of the wing. All of these tools were used to explore how the distributed propellers impacted wing aerodynamics, specifically in terms of three-dimensional aerodynamic coefficients and sectional pressure distributions, across three flap angles and four different propeller placements.

The wing model included three electric motors, each driving a propeller. These motors had dedicated load cells and could be adjusted along the longitudinal plane to explore different configurations. This setup was designed to minimize aerodynamic interference while directly measuring the propulsive forces. A representation of the motor group assembly and nacelle can be shown in Figure 2.1.

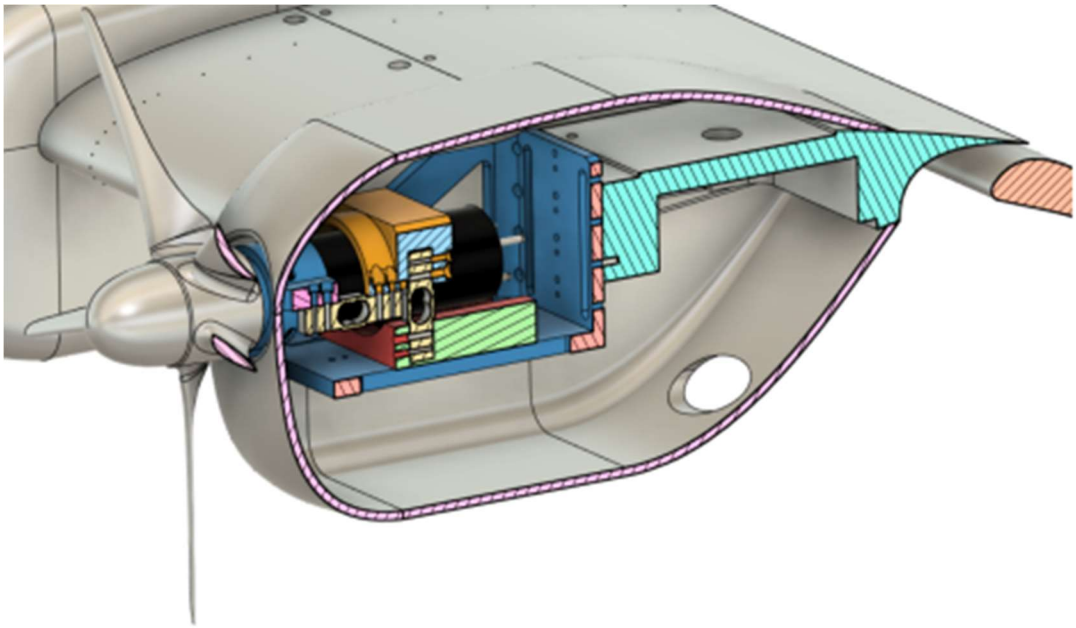

Figure 2.1 *– Motor assembly and nacelle.*

However, this arrangement required a larger motor support frame and additional electronics for signal conditioning and motor control. These components, along with power and data cables, were placed inside the wing, leading to an increase in weight and limited available space for routing cables, including those for the pressure taps to measure the dynamic pressure on the wing.

As the RPM increased, challenges had to be faced. At more than 4200 RPM, vibrations – attributed to structural resonance – started to appear in the motor assembly and limited stiffness of the load cells, which measured forces below 10 N per propeller.

These vibrations limited the maximum motor speed, that could potentially be up to 7000 RPM. It affected the motor assembly, the wing, and the external wind tunnel balance at various frequencies that could not be isolated, leading to possible dangerous scenarios. Resonance could in fact even lead to the destruction of the entire experimental setup if not considered.

For the nacelle design, a single body was created to accommodate all tested propeller positions. This approach ensured that aerodynamic and propulsive effects depended solely on the wing-propeller positioning, rather than nacelle shape, resulting in a larger nacelle that could envelop all motor placements.

Figure 2.2 *– Whole experimental setup in the wind tunnel*

The nacelle nose was modified to fit each specific propeller position both horizontally and vertically. Instead of being optimized for thrust, the propeller blade shape was chosen to produce a uniform airflow over the wing. In fact, the primary goal of the distributed propellers was to enhance the wing's lift coefficient, blowing on the wing at a given angle of attack and flight speed.

The three high-lift propellers with 0.3 m diameters were designed to blow air across the wing within the flap's span. The wing model was mounted on the sidewall of the wind tunnel test section, which served as a symmetry plane. The angle of attack was changed by an electric motor outside the wind tunnel, whose shaft was inserted in the root section of the wing model. The electric motor was installed on the external wind tunnel balance, which measured the total aerodynamic forces and moments.

Each motor was then equipped with four off-center load cells arranged orthogonally within the motor frame, as well as a temperature sensor and an RPM counter connected to a frequency-to-voltage converter. Load cells were positioned vertically to measure thrust, and two were installed horizontally to measure the normal force exerted by each propeller.

The entire structure of the experimental setup is shown in Figure 2.2. Calculations were done considering a mean aerodynamic chord $\bar{c}$ of 0.4 m (same as the root chord c_r as the wing is straight, untapered and untwisted) and a wing planform area S of 0.592 m^2.

3. Implemented methods

In this chapter, the effects of distributed propulsion on aerodynamic coefficients, using data obtained in the wind tunnel, will be explored. The objective of this analysis is to clean the wind tunnel data and identify both the direct and indirect effects of distributed propulsion. Given the presence of errors in the raw propulsion data, a methodology that leverages notes taken during the experiments has been adopted in order to reconstruct the original wind tunnel balance measurements.

In fact, there are two main sources of errors in the propulsive data, which have been divided into two main categories: *"recorded"* data, obtained directly from the sensors (motors' load cells) during the experiments and recorded by the data acquisition software, and *"annotated"* data, which were manually documented in a notebook and result more consistent with live experimental observations. In the following, the italic words *recorded* and *annotated* data refer only to the propulsive data.

As a matter of fact, some of the *recorded* data showed significant uncertainties as well as obvious anomalies. This made challenging to draw reliable conclusions about the aerodynamic effects under the influence of distributed propulsion by just using *recorded* data.

Thus, to address these errors, the *annotated* data were gathered. These were derived from a careful transcription during the experiments and definitely showed closer alignment with expected results with respect to *recorded* data. They were collected during the experiments by comparing the difference between the measured aerodynamic forces in prop-on vs. prop-off conditions, inferring the thrust and the propeller normal forces measured by the motors' load cells at low angles of attack.

Recorded and *annotated* data matched quite well in the first experiments. However, the quality of *recorded* data degraded over time, showing apparent errors in several tests. The specific causes of these faulty propulsive measurements are unknown. The same errors were not replicable by static measurements with propeller stopped. For this reason, the *recorded* data were quickly discarded in the post-processing analysis of the experiments.

As stated previously, the *annotated* data were then collected by observations and comparison with the first wind tunnel runs. However, *annotated* data are not free from errors, especially on the normal force that showed an unusual trend with angle of attack. This was attributed to the

installation layout shown in Figure 2.1. The motor was substantially hung on orthogonal springs (the off-center load cells measuring thrust and normal forces) from its front side. This configuration performed well with static measurements during the tare process but could lead to weird results when the propeller was rotating.

The wing aerodynamic coefficients in power on conditions were evaluated by including the *annotated* propulsive forces. The global measurements of the external wind tunnel balance, which included the sum of aerodynamic and propulsive forces, were lost. The aerodynamic coefficients written in the output files of the prop-on tests are representative of the indirect aero-propulsive (i.e. blowing) effects evaluated with the *annotated* data, which – as previously stated – presented some erroneous trends.

To cancel these errors, the data acquisition process was manually reversed in a spreadsheet file. The *annotated* data, which were subtracted from the wind tunnel balance measurements to get the wing aerodynamic coefficients under propeller blowing during the experiments, were summed to the same aerodynamic forces to get back to the original lost total forces, which are independent from the motors' load cells measurements. The scheme of Figure 3.1 should clarify this process.

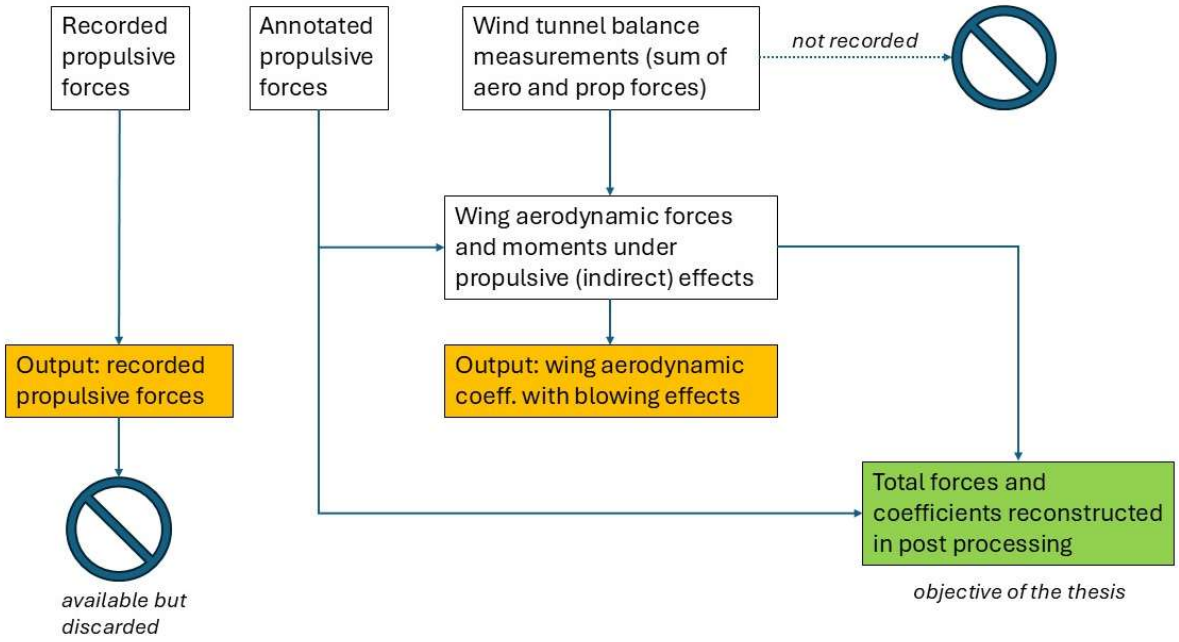

Figure 3.1 *– Scheme of the procedure used for the reconstruction of total forces and coefficients.*

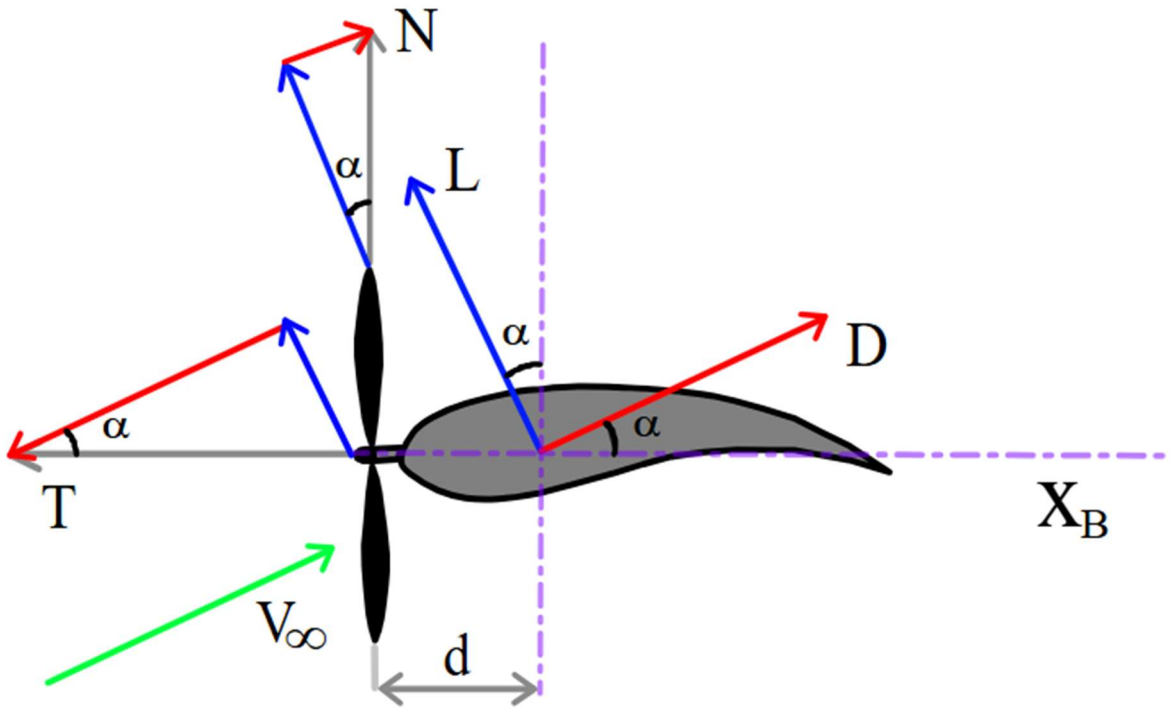

Figure 3.2 *– Wing representation for the calculation of the total forces involved.*

Figure 3.2 shows an illustration of the forces' directions (thrust and normal force are shown in gray, while vector components are blue and red colored). The total aerodynamic coefficients $C_{L,\text{tot}}$ and $C_{D,\text{tot}}$ were then obtained by dividing the total amount of lift, drag, thrust and normal force by the reference surface of the wing and the dynamic pressure.

The following equations show the procedure for the calculation of the total lift and total drag, followed by their respective total aerodynamic coefficients. L and D represent the wing aerodynamic forces under propulsive indirect effects that need to be summed to *annotated* propulsive forces in order to obtain L_{tot} and D_{tot}:

$$L_{\text{tot}} = L + T\sin\alpha + N\cos\alpha \tag{3.1}$$

$$D_{\text{tot}} = D - T\cos\alpha + N\sin\alpha \tag{3.2}$$

$$C_{L,\text{tot}} = \frac{L_{\text{tot}}}{q_\infty S} \tag{3.3}$$

$$C_{D,\text{tot}} = \frac{D_{\text{tot}}}{q_\infty S} \tag{3.4}$$

The pitching moment on the wing was evaluated afterwards. By utilizing pitching aerodynamic moment measurements, the total pitching moment was then obtained following this procedure. The moment induced by the direct effect of the normal force was easily obtained by multiplying the normal force by its arm *d* and was then subtracted to the pitching aerodynamic moment of the wing. Once the total pitching moment had been derived, it was then scaled as follows, using the reference surface of the wing, the dynamic pressure as well as the mean aerodynamic chord $\bar{c}$ to obtain the total pitching moment coefficient $C_{M,\mathrm{tot}}$:

$$M_{\mathrm{tot}} = M - Nd \tag{3.5}$$

$$C_{M,\mathrm{tot}} = \frac{M_{\mathrm{tot}}}{q_\infty S \bar{c}} \tag{3.6}$$

In the next chapter, after a discussion on the results, a numerical model of the propeller will be presented and exploited to estimate the direct and indirect propulsive effects of this configuration. The final hybrid model (experimental and numerical) will be a first step in the accurate evaluation of DEP aero-propulsive effects until dedicated experimental tests on the isolated motor group are available.

For a few missing data, averaging or interpolating between the available values was done. The obtained curves refer to different propulsion scenarios, regarding four different angular velocities, going from less than 200 RPM (with the propellers rotating under the effect of the wind and braked by the electric motor, achieving a condition similar to the prop-off configuration) up to 4200 RPM.

During the experimental tests, propellers were mounted in four different locations over the wing leading edge as seen in Figure 3.3 in order to see the different effects generated by changing the positions of the engines. Still referring to Figure 3.3: WN1 represents the central location of the engines (at $\Delta X = \Delta Z = 0$), WN2 is located 20 mm above the central position, while WN3 is located 20 mm below the central position; WN4 only has a horizontal displacement instead, located 40 mm ahead of the central position, leading to an arm augmentation, that must be considered in the calculation of the pitching moment generated by the total normal force. These displacement are in the order of 10% to 20% of the mean aerodynamic chord length.

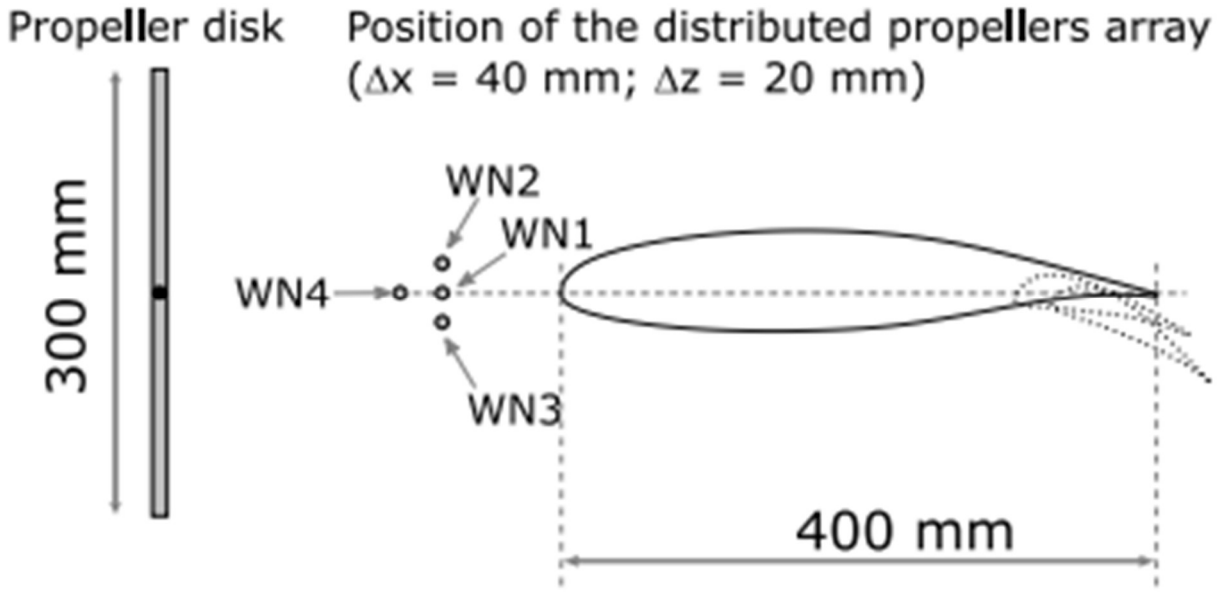

Figure 3.3 *– Analyzed propellers' array locations.*

Each location has been analyzed in at least two different flap configurations. The central position was examined at three different flap angle deflections: $\delta_f = 0°, 15°, 30°$; while the other positions at just two: $\delta_f = 15°, 30°$. This was made to highlight the different effects of distributed propulsion, simulating three different phases during flight: such flap deflection angles are typical flap configurations in cruise, take-off and landing respectively. Table 1 contains all the information specified above.

WN	**Propellers location**	**ΔX (mm)**	**ΔZ (mm)**	**δ_f (deg)**
WN1	Horizontal center, Vertical center	0	0	0º, 15º, 30º
WN2	Horizontal center, Vertical up	0	20	15º, 30º
WN3	Horizontal center, Vertical down	0	-20	15º, 30º
WN4	Horizontal forward, Vertical center	-40	0	15º, 30º

Table 1 *– Propellers' locations and flap deflection angles.*

4. Results

The approach of using *annotated* data to construct aerodynamic coefficient curves has been effective in reducing uncertainty of the results. In fact, by constructing the aerodynamic coefficient curves based on reliable data, it was possible to obtain clearer insights into the impact of distributed propulsion and the great advantages that can bring in future applications.

The analysis demonstrated that distributed propulsion has a great influence on aerodynamic coefficients on the wing, especially regarding lift, drag and pitching moment coefficients. Charts of the lift, drag and pitching moment coefficients at different RPM and propellers' array positions will be compared dividing them into three different flight configurations associated with the three different flap deflection angles ($\delta_f = 0°, 15°, 30°$).

Results will be presented in this order: general considerations about the effects of distributed propulsion on $C_{L,\text{tot}}$, $C_{D,\text{tot}}$ and $C_{M,\text{tot}}$ will be done only referring to the first propellers' array position WN1. Considerations about the differences between the different propellers' array positions will be done afterwards, comparing the different curves at maximum RPM.

4.1 Cruise configuration (Flaps retracted, $\delta_f = 0°$)

A cruise condition was analyzed with the WN1 configuration as seen in Figure 4.1. It is clear that in the linear range of the lift curve, there is an increment of both the lift coefficient $C_{L,\text{tot}}$ (much more significant) and its slope $C_{L\alpha,\text{tot}}$ (small increase). The total lift coefficient at $\alpha = 0°$, i. e. $C_{L0,\text{tot}}$, increases of about 0.05 in respect to prop-off condition; larger differences can be appreciated in take-off and landing configurations.

This is attributed to the additional local flow velocity due to the propellers' blowing behind them, providing more lift force for a given angle of attack and planform area. As RPM increase, each propeller generates a localized increment in airflow velocity over the wing surface.

This accelerated airflow effectively increases the local dynamic pressure, leading to an enhancement of lift according to Bernoulli's principle. Still referring to Figure 4.1, it is evident that, through the different RPM, the most significant augmentation of the total lift coefficient occurs between the prop-off and the prop-on curves, while among the other three curves there is a much less appreciable difference.

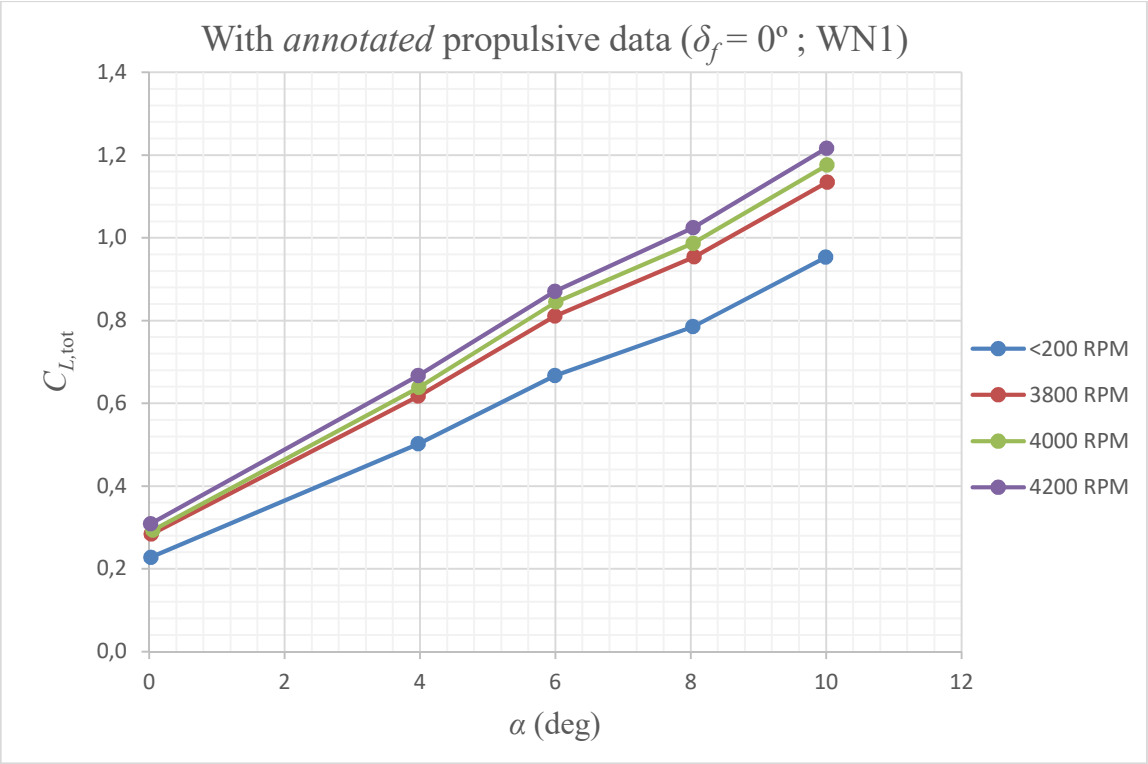

Figure 4.1 *– Total lift coefficient at* $\boldsymbol{\delta_f = 0°}$ *(cruise configuration) at WN1.*

In fact, distributed propulsion has gained significant interest especially for its big potential to enhance aircraft performance, particularly during the critical phases of take-off and landing, where velocity has to be lower and there is a need to augment the lift coefficient, compensating for the necessary amount of lift in those phases of flight.

Positioning multiple engines along the leading edge of the wing can in fact ensure a considerable improvement in lift generation, especially at lower speeds. The additional thrust close to the wing surface can create a higher local airflow, boosting the lift coefficient, allowing the aircraft to achieve lift-off at lower speeds.

The enhanced lift at lower speeds means the aircraft can reach the necessary lift conditions with a shorter runway. This reduction in take-off distance is particularly advantageous for operations that need to be performed on shorter airfields or in conditions where rapid altitude gain is necessary.

Regarding the drag coefficient, shown in Figure 4.2, the analysis shows that the total drag coefficient $C_{D,\text{tot}}$ decreases when the engines are powered on, which might initially appear contrary to the typical effects of distributed propulsion.

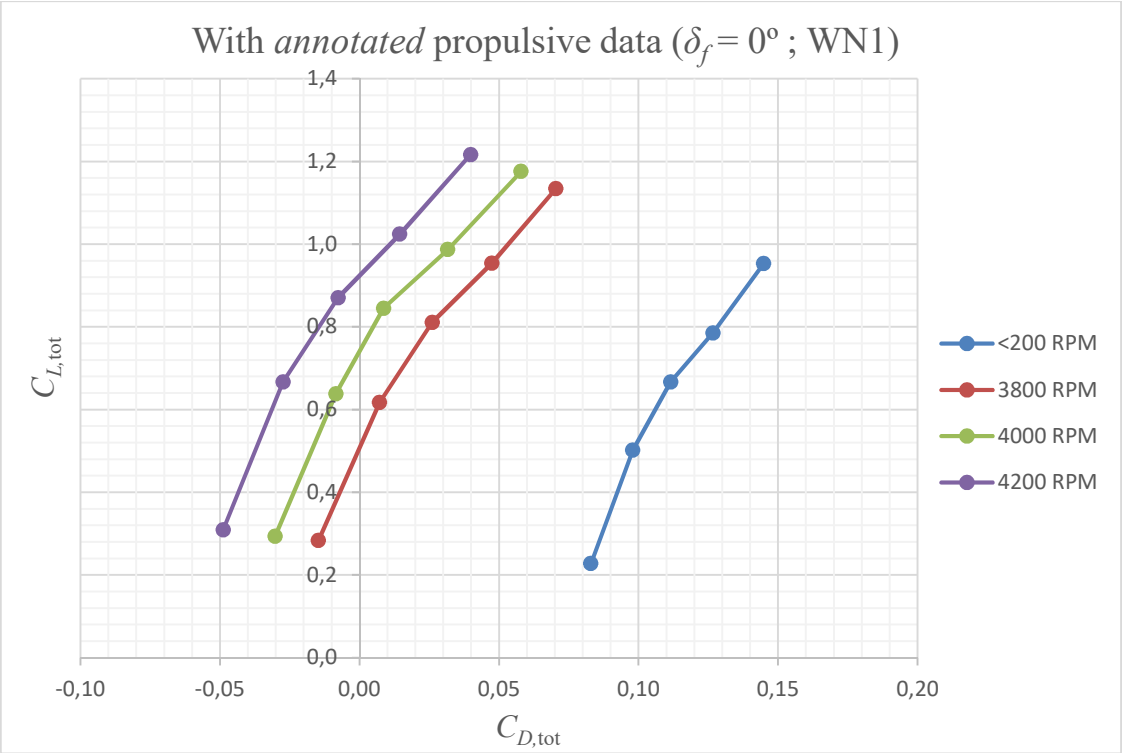

Figure 4.2 *– Total drag coefficient at* $\boldsymbol{\delta_f = 0°}$ *(cruise configuration) at WN1.*

Generally, with active distributed propulsion, an augmentation of the drag coefficient would be expected, due to the added induced drag from the enhanced lift (as part of the drag coefficient is proportional to the square of the lift coefficient C_L^2) and any potential parasite drag associated with multiple engine nacelles.

However, this apparent reduction of the drag coefficient can be explained by the influence of thrust in the calculation of the total drag coefficient. In this configuration, the total drag coefficient includes the effects of thrust, which effectively reduces the net drag when the engines are active.

As the distributed propulsion system provides additional thrust, this thrust component reduces the overall aerodynamic drag that would otherwise be larger due to the presence of higher lift induced drag. This results in a net decrease in the total drag coefficient $C_{D,tot}$ as the thrust counters a portion of drag. This is the reason why the curves tend to shift left (instead of right as it would be expected) as the RPM increase, due to the presence of higher thrust that diminishes the effects of drag itself.

For what concerns the total pitching moment coefficient $C_{M,tot}$, analysis shows that, similarly to the lift coefficient, it increases in magnitude and slope too when propellers are active as shown in Figure 4.3. This represents a common feature among all the curves in every configuration

but, in cruise condition at $\delta_f = 0°$, this trend starts to appear more evident at higher angles of attack.

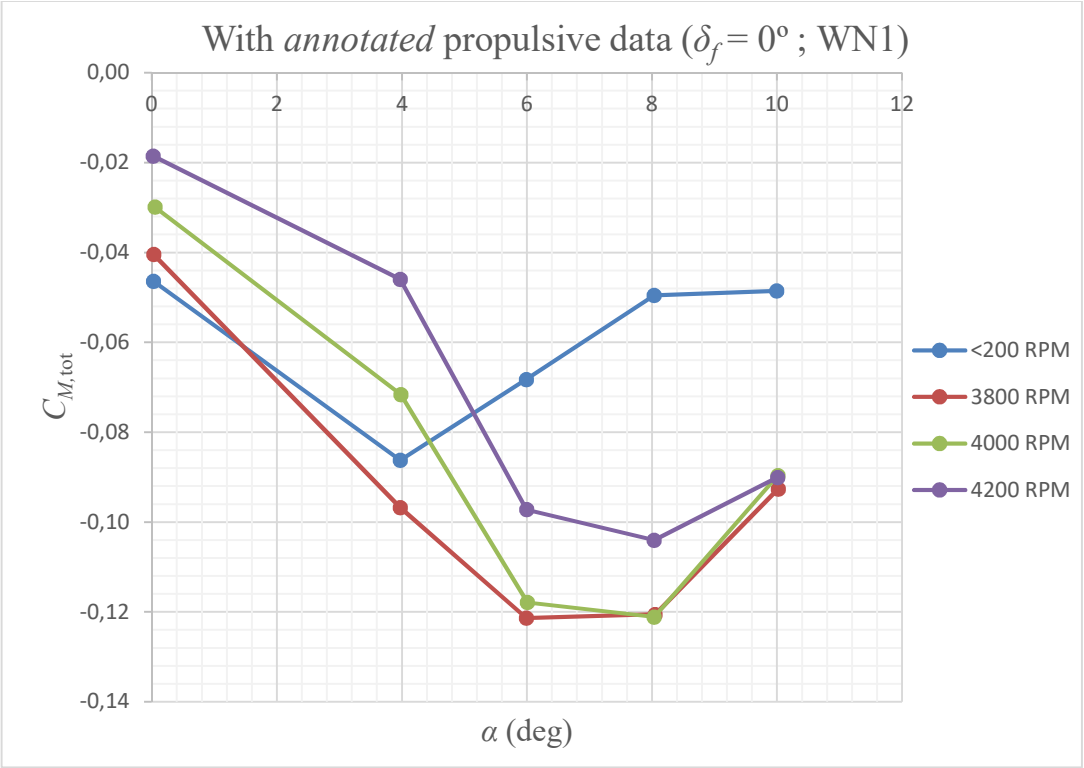

Figure 4.3 *– Total pitching moment at* $\boldsymbol{\delta_f = 0°}$ *(cruise configuration) at WN1.*

This magnitude augmentation is important for the aircraft's longitudinal flight characteristics: the magnitude of the pitching moment coefficient directly affects the performance of the aircraft, specifically the longitudinal controllability at high angles of attack. In fact, the slope of the wing pitching moment coefficient $C_{M\alpha}$ affects the aircraft longitudinal static stability. From the designer's point of view, the distributed propulsion will of course affect the sizing of both the wing and the horizontal tail.

The effects of the distributed propulsion among the prop-on curves of the total pitching moment coefficient seem to follow this trend: as the RPM of the propellers increase, the total pitching moment coefficient $C_{M,\text{tot}}$ decreases in magnitude. This is attributed to the presence of a larger normal force generated by the propellers, which acts with a nose-up pitching moment that contrasts the nose-down moment generated by the wing.

4.2 Take-off configuration (Flaps at $\delta_f = 15°$)

In this subsection, flaps are now deflected with an angle of deflection $\delta_f = 15°$, a condition that resembles take-off configuration. During take-off, flaps are typically deployed to a low angle to increase lift while limiting drag. This helps shorten the take-off roll, without excessively penalizing climb performance.

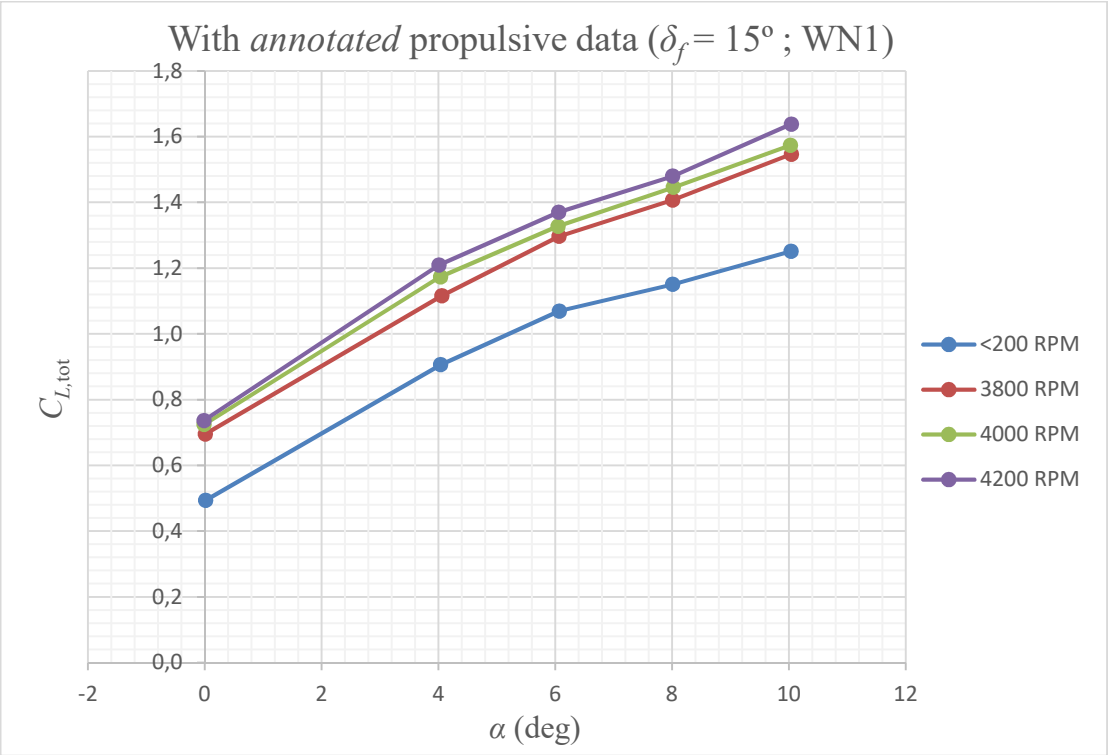

Figure 4.4 *– Total lift coefficient at* $\boldsymbol{\delta_f = 15°}$ *(take-off configuration) at WN1.*

As in the case of the clean wing, distributed propulsion increases the magnitude and the slope of the lift and pitching moment coefficients with respect to the angle of attack. As a difference, it can now be observed that DP has the effect of an additional flap deflection that further increases the coefficients. As shown in Figure 4.4, the total lift coefficient experiences a larger augmentation due to a stronger curvature of the profiles along the wing. $C_{L0,\text{tot}}$ starts from a value of approximately 0.5 and reaches 0.7 or 0.75 leading to a 40% or even 50% increment at maximum RPM.

Deflected flaps obviously create a further increment in maximum lift, which becomes useful as this will further reduce the take-off distance for a given wing planform area with respect to the unblown wing (as already discussed in the previous subsection). The gap between the prop-off and the first prop-on condition at 3800 RPM is larger, still due to the presence deflected flaps.

The total drag coefficient, shown in Figure 4.5, experiences a net increment in its magnitude. Due to the augmentation of lift, induced by the presence of deflected flaps, drag tends to increase (both for the increasing lift, leading to higher induced drag, and higher parasite drag), the curves shift right and move upwards. This trend is similar throughout all the propellers' array positions (as expected, flaps always induce higher amount of drag in every configuration). As an example, the total drag coefficient at $C_{L,\text{tot}} = 1$ starts from a value of approximately 0.14 in prop-off condition and reaches 0.01 in prop-on condition at maximum RPM (giving a 0.13 decrement in magnitude due to the direct effects of thrust).

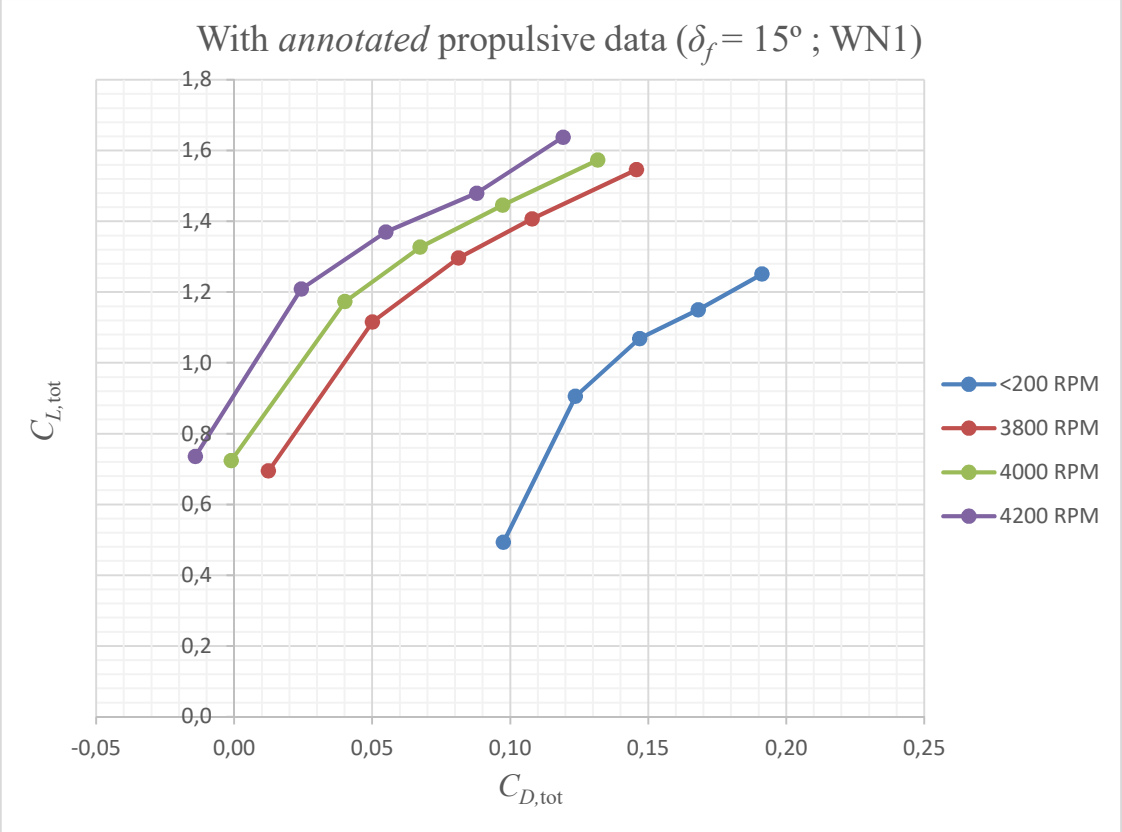

Figure 4.5 *– Total drag coefficient at* $\boldsymbol{\delta_f = 15°}$ *(take-off configuration) at WN1.*

The presence of a flap deflection also influences the total pitching moment coefficient, which increases its magnitude as shown in Figure 4.6, giving the wing a stronger tendency to pitch down. This is a typical tendency that can be appreciated when flaps are deflected: in fact, flaps tend to increase the camber and (sometimes) the effective surface area of the wing (especially fowler flaps), which boosts the lift generated by the wing.

This additional lift is concentrated towards the trailing edge of the wing, causing the center of pressure (the point where the resultant lift force acts) to shift back. Consequently, this rearward

shift can create a stronger nose-down (pitching) moment. Naturally, the change in the pitching moment caused by flap deployment often requires adjustments to the aircraft's stabilizing and control surfaces (at the horizontal tail) to maintain longitudinal equilibrium.

As already said in the previous subsection (similarly to cruise condition), when the RPM increase, the curves tend to move upwards, leading to the assumption that the total normal force generates a moment that contrasts the nose-down pitching moment of the wing. This time though, the curves experience a much less appreciable (but still clearly visible) upshift, due to a stronger nose-down pitching moment generated by the flapped wing. The total pitching moment coefficient at $\alpha = 0°$, i. e. $C_{M0,\text{tot}}$, shifts from approximately −0.13 in prop-off condition up to −0.17 at 3800 RPM decreasing of about 30%.

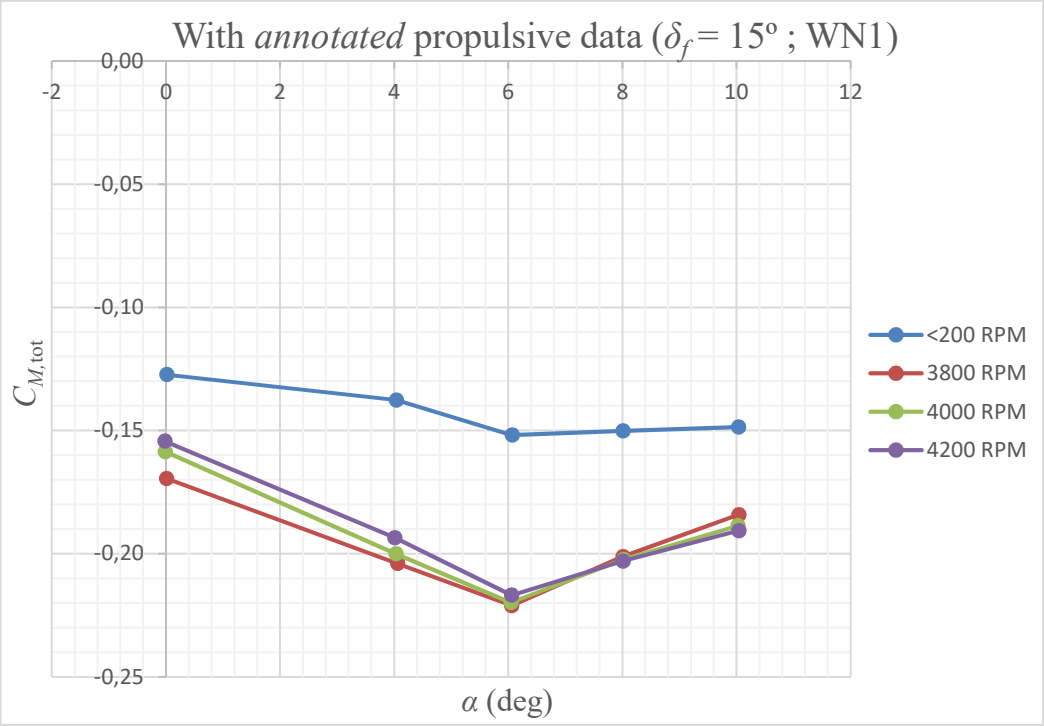

Figure 4.6 *– Total pitching moment coefficient at* $\boldsymbol{\delta_f = 15°}$ *(take-off configuration) at WN1.*

4.3 Landing configuration (Flaps at $\delta_f = 30°$)

In this final subsection landing condition will be analysed. In this configuration flaps are now deflected at $\delta_f = 30°$. During landing, higher flap deflections are used to maximize lift and drag to allow for steep approaches and slower touchdown speeds.

The effects already presented in the previous two subsections now become much stronger in landing configuration, due to the presence of a larger flap deflection angle. Flaps are now fully

deployed to achieve the highest possible C_L, allowing for low-speed, high-lift operation during approach and landing phases.

Thus, as shown in Figure 4.7, the total lift coefficient experiences an even further augmentation; the effects of distributed propellers are still the same: $C_{L,\text{tot}}$ clearly increases when the RPM increase. $C_{L0,\text{tot}}$ experiences an augmentation up to 50%, shifting from approximately 0.9 to 1.35 at maximum RPM. In fact, as already discussed in the previous subsections, the effects of DP can be seen as a further flap deflection on the wing, leading to an amplification of the lift coefficient, accompanied by drag augmentation.

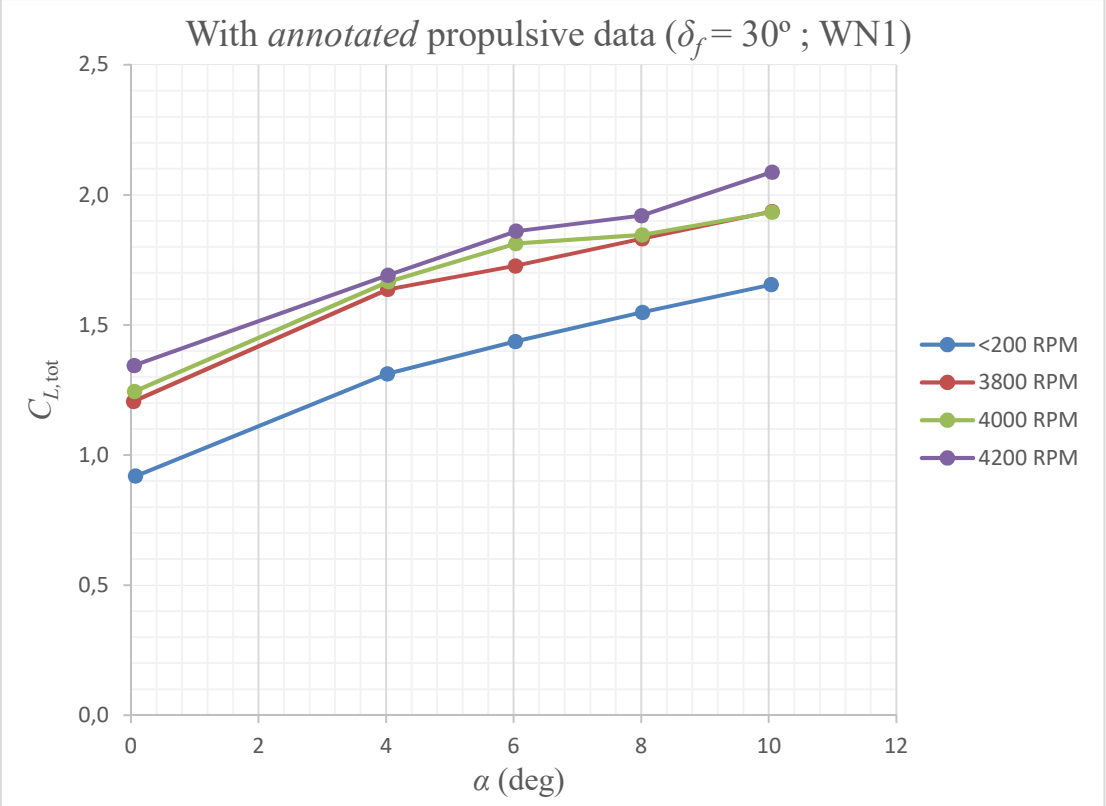

***Figure 4.7** – Total lift coefficient at $\boldsymbol{\delta_f = 30°}$ (landing configuration) at WN1.*

The total drag coefficient shown in Figure 4.8 experiences the same trends discussed in the previous two subsections, with a further drag increment. In fact, the curves tend to shift right even more, still due to the presence of a larger flap deflection.

This actually becomes useful during landing phase as more resistance against the forward motion is generated. This helps the aircraft to slow down faster augmenting the deceleration. Moreover, especially during landing, the aircraft needs to reduce its speed to a safe level before touchdown. A higher drag coefficient can help maintain a more controlled descent by increasing the aircraft's rate of deceleration without requiring excessive use of the brakes or other method.

Thus, the aircraft can reach a lower, safer speed before reaching the runway, minimizing the risk of overshooting the runway or not stopping in time. This is particularly beneficial in short-runway scenarios where precise speed control is critical.

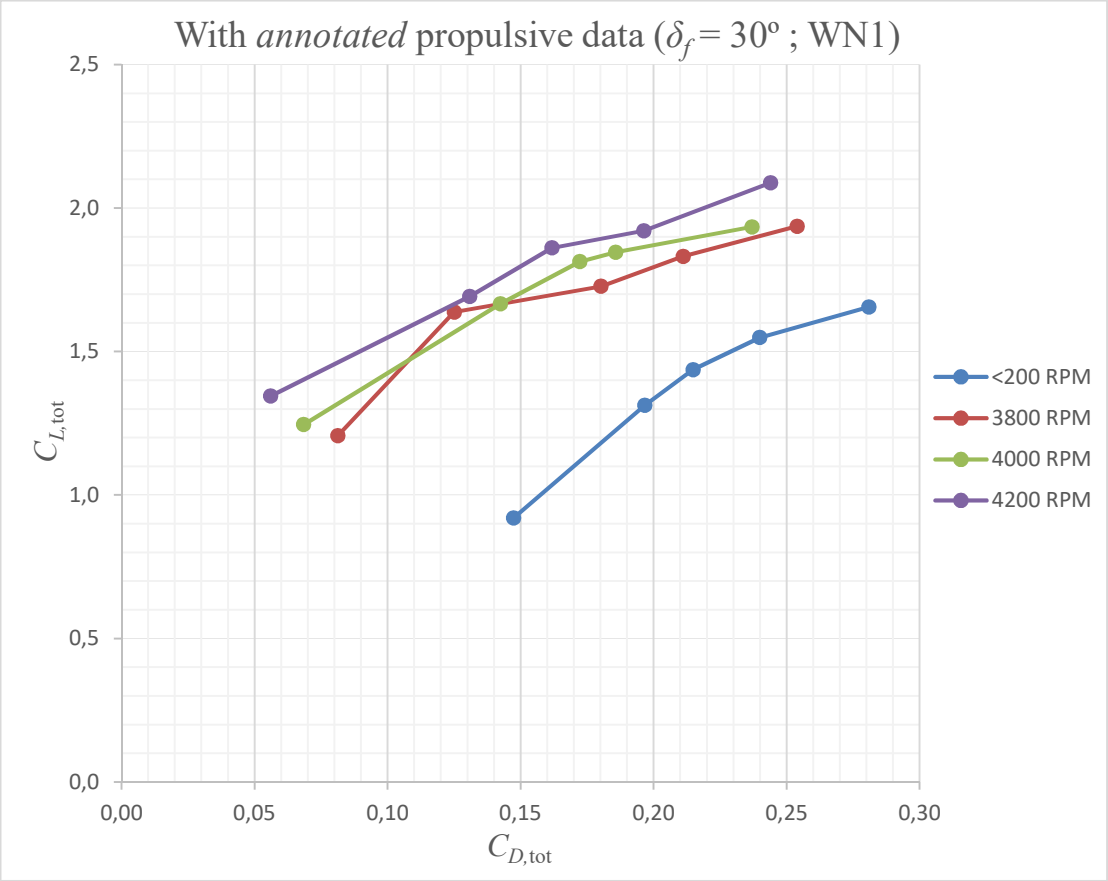

Figure 4.8 *– Total drag coefficient at* $\boldsymbol{\delta_f = 30°}$ *(landing configuration) at WN1.*

The total pitching moment coefficient, shown in Figure 4.9, still follows the same trends, with a clear and considerable further amplification in its magnitude, as landing configuration is being analyzed. The curvature of the airfoils along the wing increases even more, leading to a stronger nose-down pitching moment (due to an even larger movement of the center of pressure towards the trailing edge).

This time, increasing the RPM leads to an opposite trend (in respect to cruise and take-off configurations): curves tend to shift down instead of up as in the two previous cases. This is because, as the RPM increase, the flapped wing experiences a stronger nose-down pitching moment which actually becomes larger than the moment generated by the total normal force.

When RPM increase, also the total normal force increases (leading to a stronger nose-up pitching moment) but, when flaps are completely deflected during a typical landing phase, there

is a much stronger nose-down contribution to the pitching moment of the wing, leading it to pitch down even more. $C_{M0,\text{tot}}$ experiences a negative increment of about 40% between prop-off and prop-on conditions, shifting from a value of −0.24 up to −0.34 at maximum RPM.

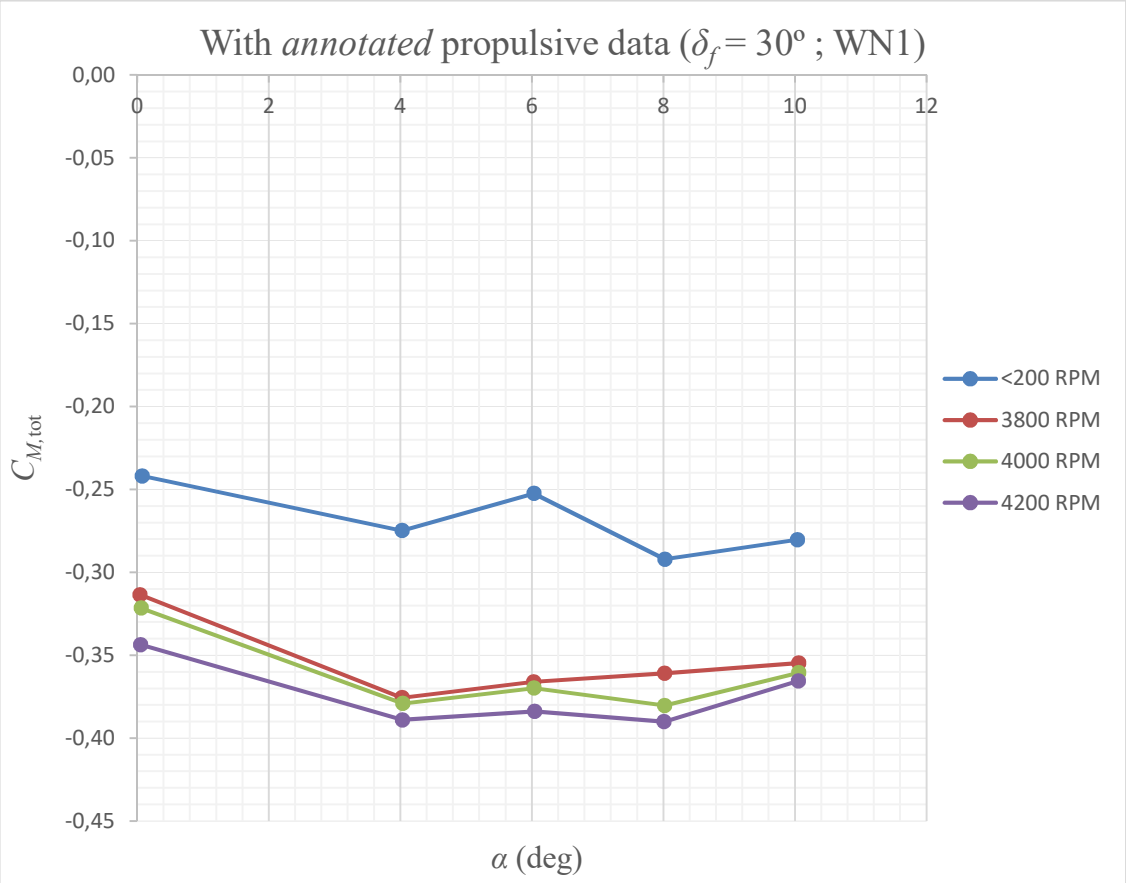

Figure 4.9 *– Total pitching moment coefficient at* $\boldsymbol{\delta_f = 30°}$ *(landing configuration) at WN1.*

4.4 Effects of the propellers' array position

Effects deriving from moving the propellers' array in the four possible positions will now be analyzed. Referring to the illustration in Figure 3.3, all four positions will be compared only in take-off and landing configurations, leaving apart cruise configuration due to missing experimental tests at $\delta_f = 0°$ for propellers' array positions WN2, WN3 and WN4 (as already specified in Table 1).

Even though data of all the analyzed propellers' array positions may not be available for cruise configuration, this is not necessarily a significant drawback. The primary advantages of distributed propulsion are in fact more evident during take-off and landing, where high thrust

demands and precise control over speed and descent are crucial. In cruise conditions, the benefits of distributed propulsion tend to diminish as the aircraft operates at higher speeds.

The constructed charts have been obtained using the same *annotated* data coming from the same experiments, here only shown at the maximum achievable angular velocity of 4200 RPM, to inspect which position would be the best among the others in terms of maximizing lift and limiting drag (also the influence on the pitching moment will be analyzed). Presented charts still represent the total aerodynamic coefficients $C_{L,\text{tot}}$, $C_{D,\text{tot}}$ and $C_{M,\text{tot}}$.

In take-off configuration, the comparison among the different curves of the total lift coefficient $C_{L,\text{tot}}$, deriving from the four propellers' array locations, is shown in Figure 4.10.

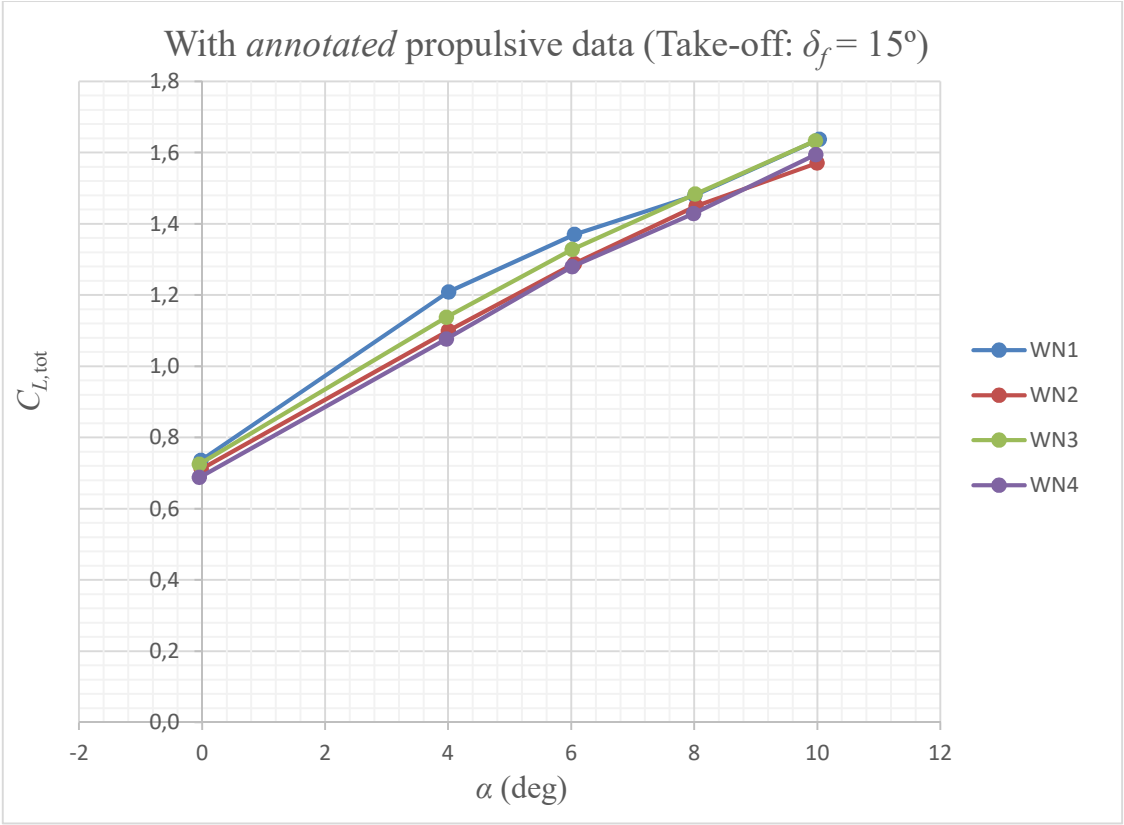

Figure 4.10 *– Total lift coefficient among the different propellers' array positions at* $\boldsymbol{\delta_f = 15°}$ *(take-off configuration).*

It seems possible to affirm that moving the propellers' array vertically or horizontally does not induce a significant variation of the total lift coefficient in take-off configuration. The analysis shows that the curve referring to WN1 reaches slightly higher values of $C_{L,\text{tot}}$, leading it to be the best propellers' position in take-off configuration, followed by WN3 (propellers positioned 20 mm below WN1).

For what concerns the total drag coefficient $C_{D,\text{tot}}$, shown in Figure 4.11, a clear difference among the several total drag coefficient curves can be observed. It seems that positioning the propellers in the upward position (WN2) induces a considerable increment of drag, leading it to be the worst propellers' position among the others in terms of aerodynamic efficiency.

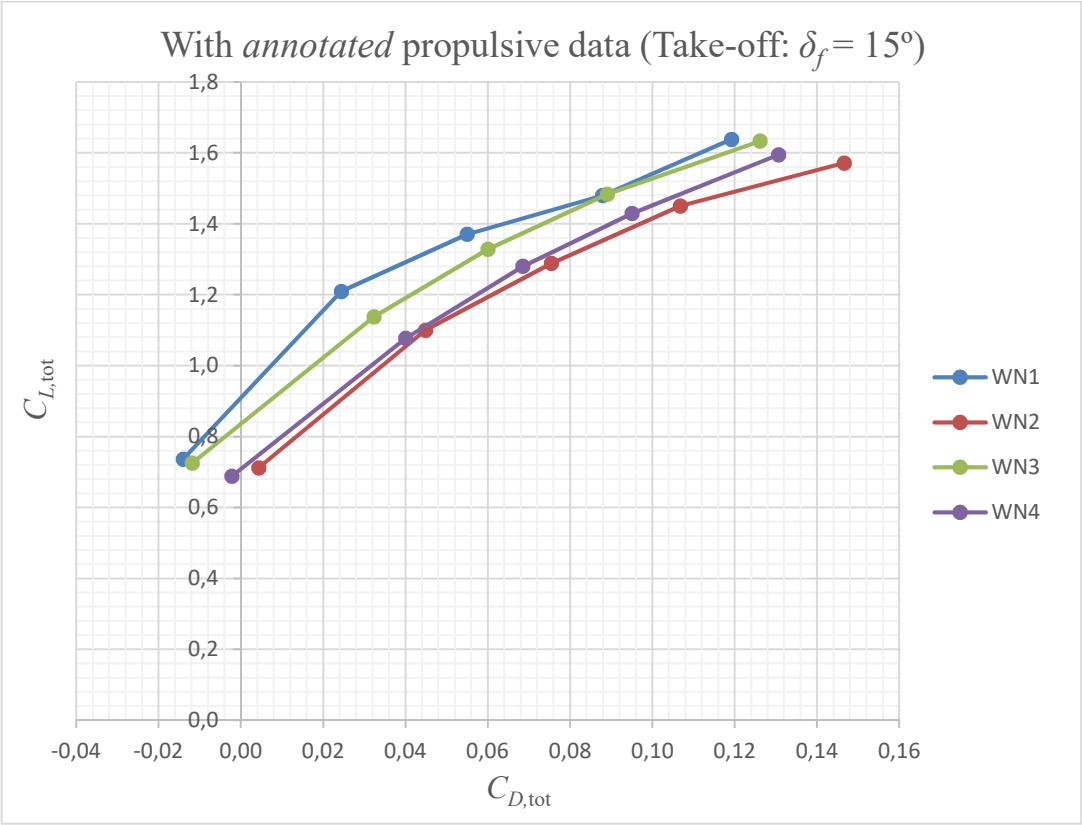

Figure 4.11 *– Total drag coefficient among the different propellers' array positions at* $\boldsymbol{\delta_f = 15°}$ *(take-off configuration).*

WN1 and WN3 still seem to be the best propellers' array positions also in terms of minimizing the effects of total drag. Thus, they can be considered the best propellers' array locations in terms of aerodynamic efficiency. It has to be taken into account that these are still considerations made on slight shifts of the curves, so the differences among them are not that influent in terms of choosing or finding the best position.

Regarding the total pitching moment coefficient $C_{M,\text{tot}}$ shown in Figure 4.12, the results of the analysis show a similar behavior between WN2 and WN4 (the same happens for $C_{L,\text{tot}}$) that are different from the behaviors of WN1 and WN3, where the most lift is produced.

In fact, the magnitude of the total pitching moment coefficient increases in those two positions with a larger pitch down tendency, i.e. $C_{M\alpha,\text{tot}}$, in WN3. Thus, WN3 seems to be the most stable position (in terms of longitudinal static stability) amongst all of the considered propellers'

locations. However, this behavior could also be linked to possible errors in the experimental measurements, leading to uncertain conclusions on the curve's slope referring to WN3 configuration.

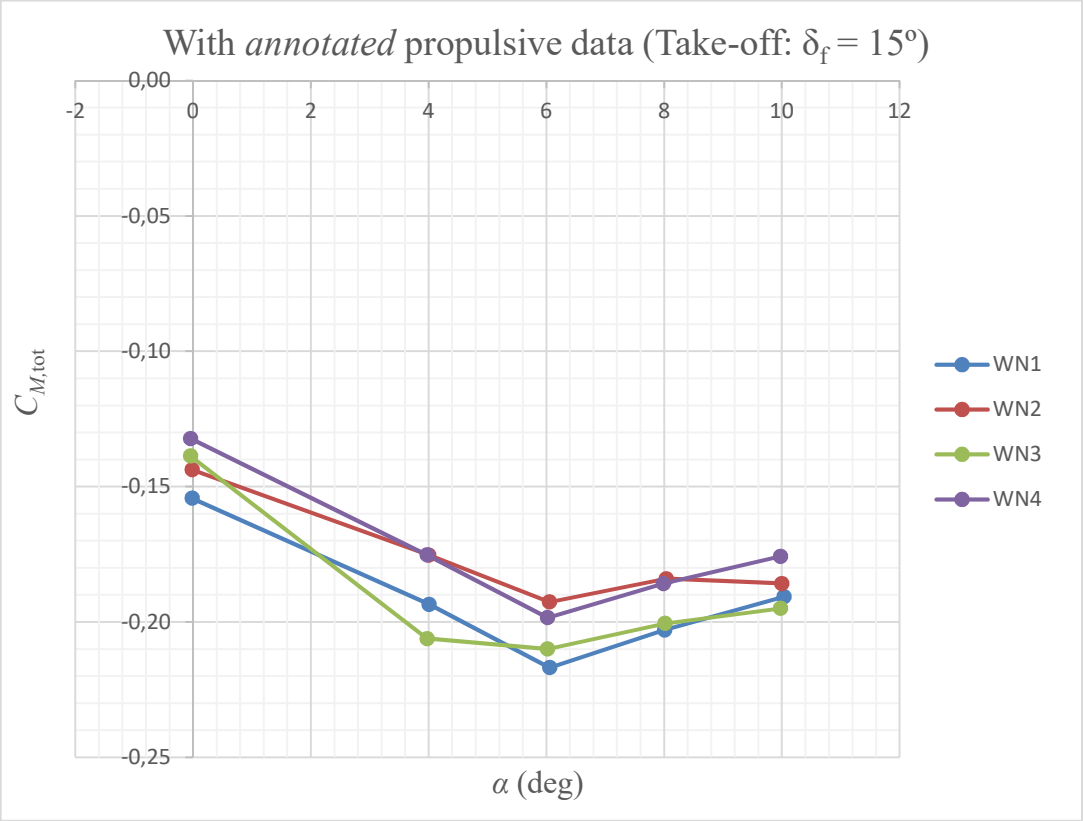

Figure 4.12 *– Total pitching moment coefficient among the different propellers' array positions at* $\boldsymbol{\delta_f = 15°}$ *(take-off configuration).*

In landing configuration, the same trends visualized in take-off configuration are observed. Clearly, as already said in subsection 4.3, the effects of distributed propulsion on a flapped wing are amplified and become even stronger when flaps are completely deflected.

As shown in Figure 4.13, WN3 curve has a larger slope $C_{L\alpha,\text{tot}}$ among the curves of other propellers' positions. In fact, if propellers are mounted under the central position (WN3), especially at higher angles of attack, the most amount of lift is produced. At lower angles of attack, WN1 is actually preferred to WN3. Also in landing configuration, these two propellers' array locations still tend to be preferred with respect to WN2 and WN4, in terms of maximizing the total lift production.

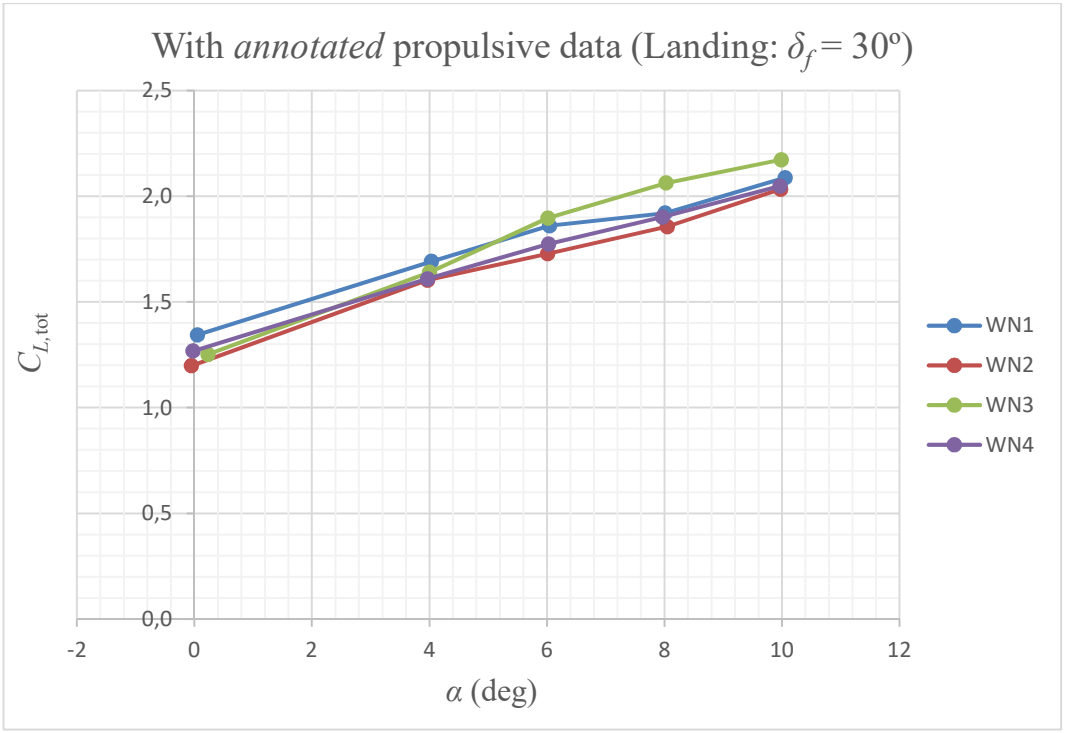

Figure 4.13 *– Total lift coefficient among the different propellers' array positions at* $\boldsymbol{\delta_f = 30°}$ *(landing configuration).*

Considering now the total drag coefficient shown in Figure 4.14, the analysis shows there is a much less appreciable difference among the curves of the different propellers' locations.

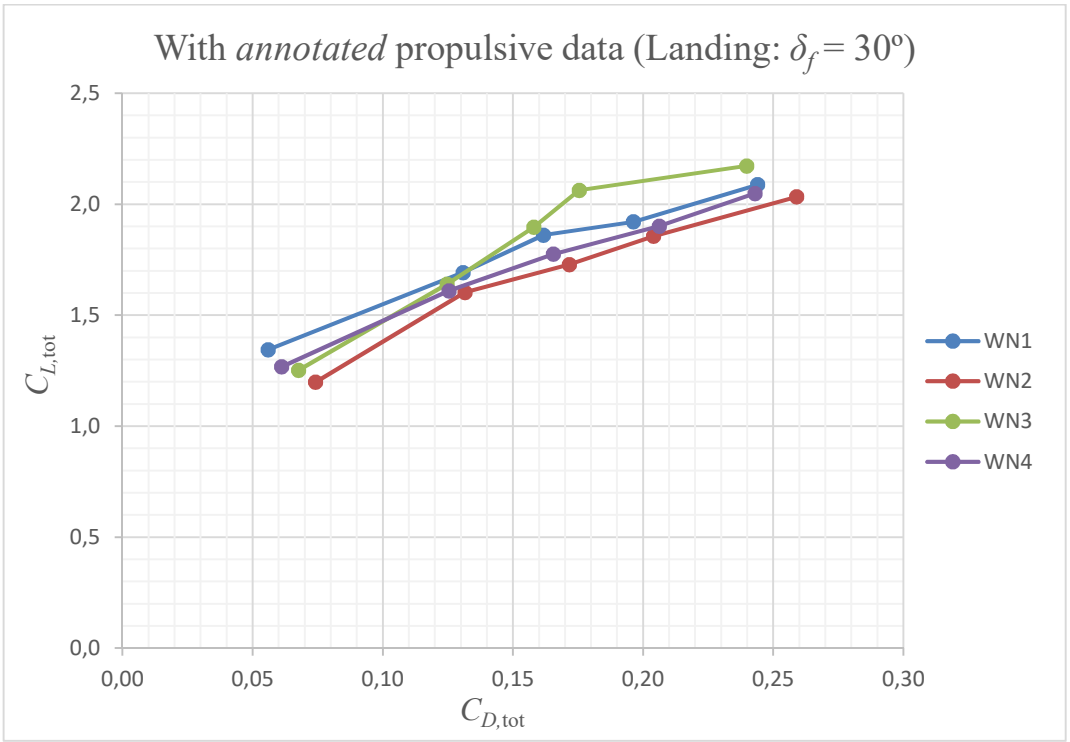

Figure 4.14 *– Total drag coefficient among the different propellers' array positions at* $\boldsymbol{\delta_f = 30°}$ *(landing configuration).*

Positioning the propellers at WN2 still seems to be the location that produces the highest value of $C_{D,\text{tot}}$. During landing phase, as already said in subsection 4.3, this position actually becomes an advantage, helping the aircraft to slow down more effectively. In fact, reducing aerodynamic efficiency can be beneficial to facilitate braking and deceleration: prioritizing drag over lift during landing also reduces the reliance on wheel brakes and shortens the landing distance.

Finally, as regards the total pitching moment coefficient in landing configuration among the different propellers' array positions, shown in Figure 4.15, the trends are similar to the already discussed ones in take-off configuration.

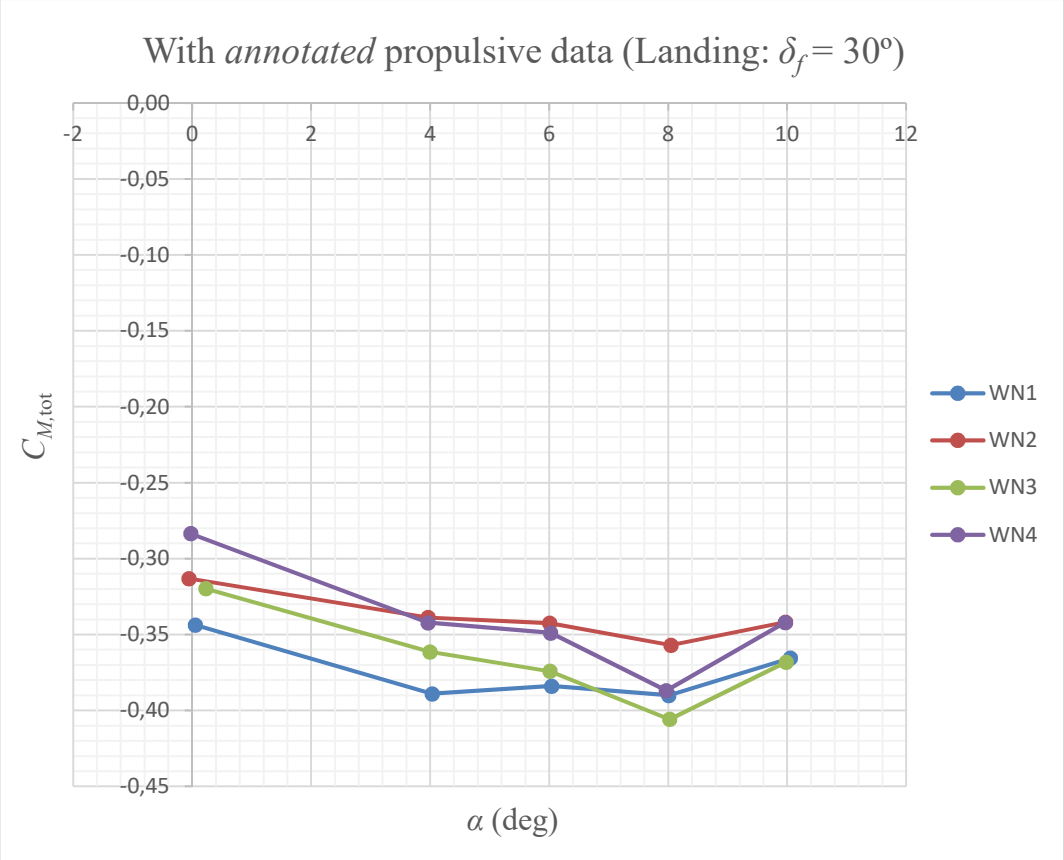

Figure 4.15 *– Total pitching moment coefficient among the different propellers' array positions at* $\boldsymbol{\delta_f = 30°}$ *(landing configuration).*

The curves referring to WN1 and WN3 are still under the ones referring to WN2 and WN4, leading to a larger magnitude of the total pitching moment in those configurations (stronger nose-down pitching moment).

4.4 Numerical Analysis

As already anticipated, in this final subsection, propulsive data coming from a numerical CFD model of the same wing will be analyzed in order to obtain and better highlight the indirect effects of distributed electric propulsion. Numerical simulations were performed on the same geometry of the WN1 at $\delta_f = 15°$ (take-off configuration) with propellers rotating at 4200 RPM. The average thrust and normal force of the three propellers have been evaluated. By assuming these propulsive data as correct, the propellers' indirect effects on the wing aerodynamics have been evaluated by simply inverting equations (3.1), (3.2), (3.5) as follows:

$$L_{\text{aero}} = L_{\text{tot}} - T\sin\alpha - N\cos\alpha \tag{4.1}$$

$$D_{\text{aero}} = D_{\text{tot}} + T\cos\alpha - N\sin\alpha \tag{4.2}$$

$$M_{\text{aero}} = M_{\text{tot}} + Nd \tag{4.3}$$

Following this procedure, total aerodynamic forces have been filtered out to exclude thrust and normal force components, isolating lift, drag and pitching moment, which now only depend on the indirect effects of distributed electric propulsion. This approach allowed for a clearer analysis of the impacts of distributed propulsion without the need to account for the direct contributions coming from propulsive effects. Consequently, the relative aerodynamic coefficients have been found still following the same procedures:

$$C_L = \frac{L_{\text{aero}}}{q_\infty S} \tag{4.4}$$

$$C_D = \frac{D_{\text{aero}}}{q_\infty S} \tag{4.5}$$

$$C_M = \frac{M_{\text{aero}}}{q_\infty S\bar{c}} \tag{4.6}$$

New charts of these coefficients have been plotted, leading to a more direct visualization of the indirect effects of distributed propulsion (completely excluding the effects deriving from propulsive contributions). In this subsection, results will obviously show lift, drag and pitching moment coefficients only at $\delta_f = 15°$ in WN1 configuration at 4200 RPM, as numerical propulsive data were only obtained for this particular configuration. The trends of the single coefficients will be compared to the curves referring to the same wing configuration in prop-off condition (here still shown at < 200 RPM).

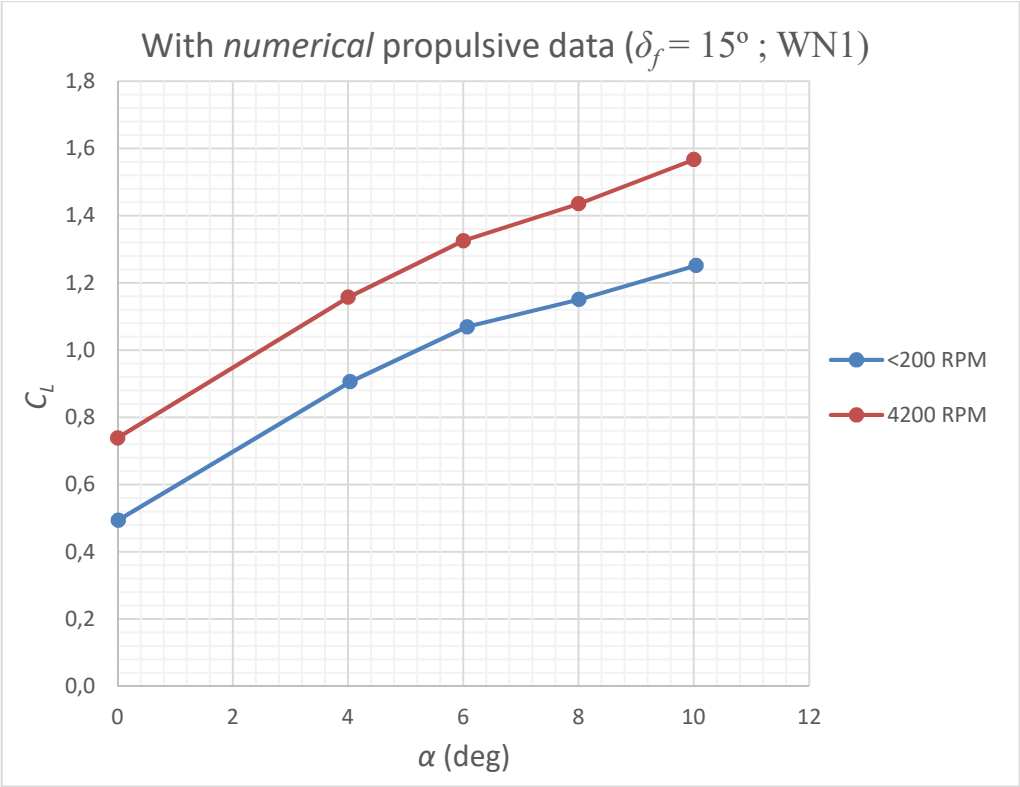

Figure 4.16 *– Comparison of the wing lift coefficient at* $\boldsymbol{\delta_f = 15°}$ *(take-off configuration) at WN1 between prop-off and prop-on conditions.*

Starting from the lift coefficient C_L, shown in Figure 4.16, the indirect effects of distributed propulsion are now much more evident. The prop-on curve clearly stands above the one referring to prop-off condition: distributed propulsion, in fact, enhances the lift coefficient by augmenting the local velocity of the airflow, energizing it over the wing. C_{L0} shifts upwards from a value of 0.48 in prop-off condition to 0.75 in prop-on condition, giving an increment of about 56%.

As already discussed in the previous chapters, this effectively improves high-lift capabilities of an aircraft at lower speeds, possibly enabling the use of smaller wings for greater high-speed cruise efficiency without compromising low-speed performance, as it is necessary during take-off and landing phases. Clearly, augmenting the high-lift capabilities of an aircraft, leads to shorter take-off and landing distances as well.

As it would be expected, the drag polar, shown in Figure 4.17, visibly moves right (and upwards, due to the lift increment) with propellers enabled. The drag coefficient C_D shifts to higher values because of the augmentation of lift induced drag, which is proportional to the square of the lift coefficient C_L^2. The drag coefficient may also increase due to an additional contribution attributed to parasite drag, related to the additional friction from the increased local

flow velocity. As an example, the drag coefficient evaluated at $C_L = 1$ obviously shifts right from a value of 0.14 in prop-off condition to 0.38 in prop-on condition (increment of about 0.24).

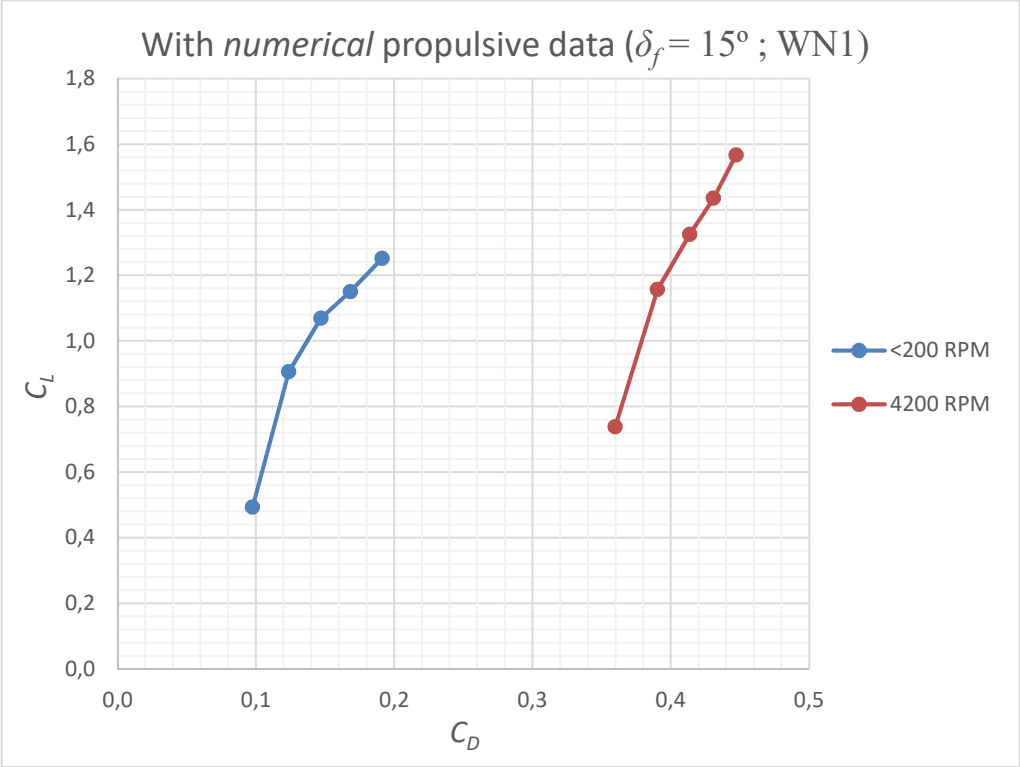

***Figure 4.17** – Comparison of the wing drag coefficient at $\boldsymbol{\delta_f = 15°}$ (take-off configuration) at WN1 between prop-off and prop-on conditions.*

Finally, the indirect effects of DEP on the pitching moment coefficient C_M are shown in Figure 4.18. As expected, due to the blowing effects of the propellers, the prop-on curve tends to shift downwards in respect to the prop-off condition. The pitching moment coefficient increases in magnitude (tending to more negative values) and slope too, leading to important consequences on the aircraft longitudinal flight characteristics, directly affecting the aircraft's performance and longitudinal stability. C_{M0} starts from a value of approximately −0.13 in prop-off condition and shifts downwards to a value of −0.15, leading to a 15% negative increment in prop-on condition.

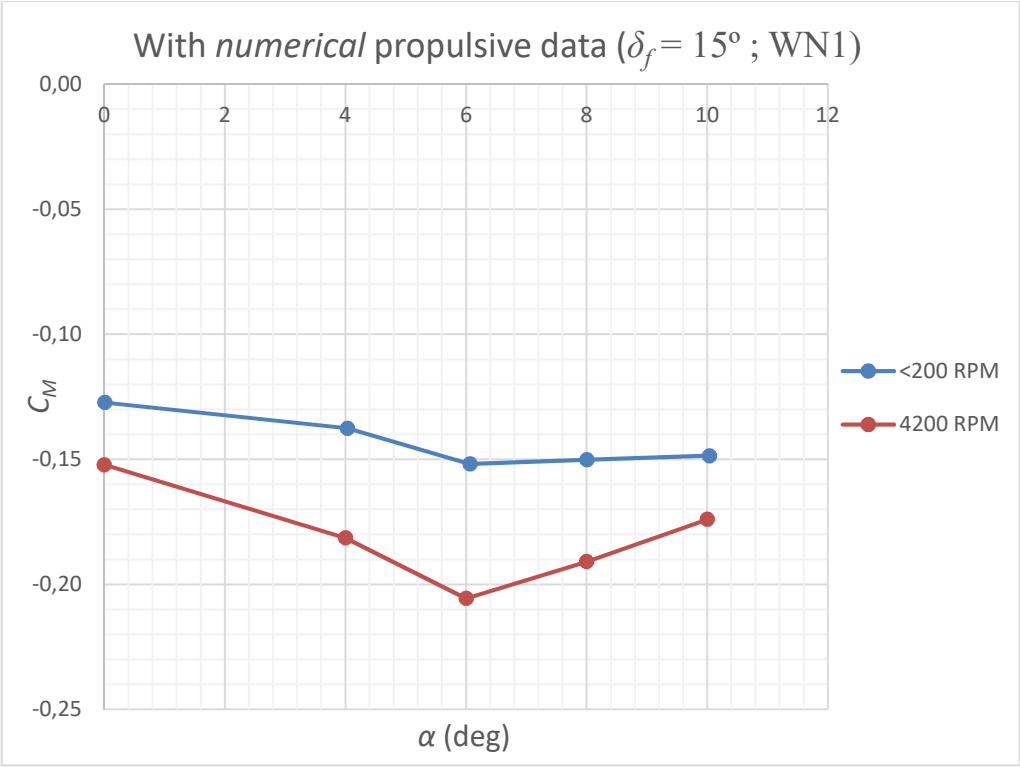

Figure 4.18 *– Comparison of the wing pitching moment coefficient at* $\boldsymbol{\delta_f = 15°}$ *(take-off configuration) at WN1 between prop-off and prop-on conditions.*

As already mentioned above, these numerical simulations were only available for take-off configuration at $\delta_f = 15°$ with propellers positioned at WN1. Same procedures and considerations can be followed developing future and newer numerical propulsive data referring to the remaining configurations (cruise at $\delta_f = 0°$ and landing at $\delta_f = 30°$) and propellers' array positions (WN2, WN3 and WN4).

5. Conclusions

By isolating indirect effects from the direct contributions of propulsion, this work has demonstrated the potential of distributed propulsion in enhancing aircraft performance. The study provided a clearer understanding of how distributed electric propulsion interacts with wing aerodynamics. The combination of wind tunnel experiments and CFD data allowed to extract the aero-propulsive indirect effects, which were missing in the original experimental data. This semi-empirical approach highlighted how flap deflection and placement of the propulsion system can influence aerodynamic coefficients (particularly lift, drag, and pitching moment coefficients).

Findings emphasized that distributed propulsion can potentially offer significant opportunities to optimize aircraft performance. Most importantly, the ability to locally energize the airflow on the wing, leading to larger values of the lift coefficient, especially useful during take-off and landing phases. Consequently, higher amount of drag can be achieved, potentially helping braking procedures during landing and leading to shorter take-off and landing lengths.

Future researches could explore even more advanced configurations of distributed propulsion systems, including its integration into blended-wing-body designs or even non-conventional aircraft geometries. Additionally, experimental validation of more complex CFD models and real flight testing could further refine a better understanding of distributed propulsion's full potential, demonstrating its value as an innovating and promising technology in modern aviation.

Bibliography

[1] Danilo Ciliberti, Pierluigi Della Vecchia, Vincenzo Orticalco, Fabrizio Nicolosi, "Aero-Propulsive Interactions between UAV Wing and Distributed Propellers Due to Their Relative Position", Department of Industrial Engineering, University of Naples "Federico II", Naples, January 2023.

[2] Garl L. Gentry, Jr., M. A. Takallu, and Zachary T. Applin, "Aerodynamic Characteristics of a Propeller-Powered High-Lift Semispan Wing", NASA Technical Memorandum 4541, April 1994.

[3] Pierluigi Della Vecchia, Daniele Malgieri, Fabrizio Nicolosi, Agostino De Marco, "Numerical analysis of propeller effects on wing aerodynamic: tip mounted and distributed propulsion", 6th CEAS AIR & SPACE CONFERENCE AEROSPACE EUROPE 2017, CEAS 2017, Bucharest, 16-20 October 2017.

[4] Kim, Hyun D., Perry, Aaron T., and Ansell, Phillip J., "A Review of Distributed Electric Propulsion Concepts for Air Vehicle Technology", NASA Armstrong Flight Research Center, Edwards, California 93523, University of Illinois at Urbana-Champaign, Urbana, Illinois 61801, July 12, 2018.

[5] Nicholas K. Borer, Joseph M. Derlaga, Karen A. Deere, Melissa B. Carter, Sally A. Viken, Michael D. Patterson, Brandon L. Litherland, Alex M. Stoll, "Comparison of Aero-Propulsive Performance Predictions for Distributed Propulsion Configurations", NASA, Joby Aviation, 2019.

[6] Andy Ko, J.A. Schetz and William H. Mason, "Assessment of the Potential Advantages of Distributed-Propulsion for Aircraft", Multidisciplinary Analysis and Design Center for Advanced Vehicles Virginia Polytechnic Institute and State University, Blacksburg.

[7] Nicholas K. Borer, Michael D. Patterson, Jeffrey K. Viken, Mark D. Moore, Sean Clarke, Matthew E. Redifer, Robert J. Christie, Alex M. Stoll, Arthur Dubois, JoeBen Bevirt, Andrew R. Gibson, Trevor J. Foster, Philip G. Osterkamp, "Design and Performance of the NASA SCEPTOR Distributed Electric Propulsion Flight Demonstrator", NASA, Joby Aviation, Empirical Systems Aerospace, Inc., 2019.